J. Fluid Mech. (2023), *vol*. 972, A18, doi:10.1017/jfm.2023.707

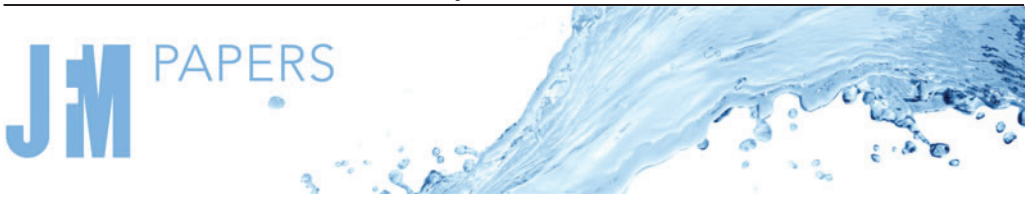

Scaling law of structure function of Richtmyer–Meshkov turbulence

Zhangbo Zhou[1], **Juchun Ding**[1],†, **Wan Cheng**[1] **and Xisheng Luo**[1]

[1]Advanced Propulsion Laboratory, Department of Modern Mechanics, University of Science and Technology of China, Hefei 230026, PR China

(Received 3 January 2023; revised 24 July 2023; accepted 21 August 2023)

The scaling law of the structure function of Richtmyer–Meshkov (RM) turbulence is investigated both numerically and theoretically. High-fidelity simulations with a minimum-dispersion, adaptive-dissipation scheme are first performed. Results show that the mixing width experiences an exponential growth and the turbulent kinetic energy has a visible $-3/2$ spectrum. The scalar field exhibits a greater degree of intermittency than the velocity field, and also the small-scale statistics suffer a larger influence of large scales. Visible differences in the scaling law of the structure function among the RM turbulence and other types of turbulence are observed, which reveal the unique characteristic of RM turbulence. A phenomenological theory, which gives the spatial and temporal scaling laws of the structure functions of velocity and scalar of RM turbulence, is developed for the first time by introducing an external agent. The spatial scaling exponents of structure functions from simulation deviate from the Kolmogorov exponents, but are quite close to the RM-modified anomalous exponents. This demonstrates the validity of the present phenomenological theory. The temporal scaling exponents of structure functions first meet the RM-modified anomalous exponents, and then approach the Kolmogorov–Obukhov–Corrsin non-intermittent ones.

Key words: shock waves, turbulent mixing

1. Introduction

Compressible turbulent mixing between two fluids of different properties is a hot topic in fundamental research and also plays an important role in natural and industrial fields such as supernova explosions (Abarzhi *et al.* 2019) and inertial confinement fusion (Casner 2021). As a typical representative of compressible turbulence, turbulence developing from Richtmyer–Meshkov (RM) instability (Richtmyer 1960; Meshkov 1969) that occurs as a shock wave impacts a corrugated interface, has become increasingly attractive in recent years. Great efforts and attempts have been made to investigate RM turbulence,

† Email address for correspondence: djc@ustc.edu.cn

and substantial progress has been achieved for low-order statistics (Mohaghar *et al.* 2019; Groom & Thornber 2021; Yan *et al.* 2022). For a comprehensive overview, readers are referred to the review of Zhou (2017).

In fully developed turbulence, the dynamics of intermediate scales is free of energy-containing scales L and dissipation scales η, and thus exhibits a universal behaviour (this range is called the inertial range). The universal behaviour of the inertial range has been the focus of the turbulence community over the past decades (Benzi & Biferale 2015). Particularly, the 4/5th law of the third-order structure function (defined as the moment of the velocity increment) in the inertial range discovered by Kolmogorov (1941*a*) is a milestone achievement in turbulence research. Today, finding the scaling law of the structure function for various types of turbulence, e.g. RM turbulence, is still a central goal for turbulence researchers.

Phenomenological theory is a useful tool to examine the structure function of RM turbulence. Compared with statistically steady turbulence, statistically unsteady turbulence (i.e. statistics of fluctuations are time dependent) is more complex, which impedes the establishment of phenomenological theory. Unlike Rayleigh–Taylor (RT) turbulence, in which large scales are forced by the continuous conversion of potential energy into kinetic energy, unforced RM turbulence gains kinetic energy solely from the shock–interface interaction, which is more difficult to investigate in experiment and simulation. Fortunately, for unsteady turbulence like RM or RT turbulence (Taylor 1950), there exists a scaling law for the growth of the mixing width (Dimonte *et al.* 2004; Thornber *et al.* 2017), which makes it possible to establish a phenomenological theory. For RT turbulence, Chertkov (2003) has derived a phenomenological theory based on the quadratic growth of the mixing width. Specifically, assuming the small-scale fluctuations adjust in a timely manner to the current kinetic energy flux, a quasi-stationary, adiabatic generalization of the Kolmogorov–Obukhov picture like that of steady turbulence is obtained (Kolmogorov 1941*b*). Then, the scaling law of the structure function of RT turbulence was obtained (Boffetta *et al.* 2010; Zhao, Liu & Lu 2020). For RM turbulence, several phenomenological theories for the power law of the energy spectrum have been developed (Mikaelian 1989; Zhou 2001). By treating equally the time scales of external agent and local nonlinear interaction and also assuming the independence of the energy flux, ε, from wavenumber, k, Zhou (2001) extended the Kolmogorov scenario to RM/RT turbulence via dimensional analysis

$$\varepsilon = C_\tau^2 \tau_{tr}(k) k^4 E^2(k), \tag{1.1}$$

where C_τ is a constant, τ_{tr} is the lifetime of the transfer function correlations and E is the energy spectrum. If τ_{tr} is substituted by the eddy-turnover time scale $\tau_{eddy} = [k^3 E(k)]^{-1/2}$, (1.1) reduces to the classical Kolmogorov spectrum $E(k) = C_K \varepsilon^{2/3} k^{-5/3}$. If τ_{tr} is substituted by the RT external time scale $\tau_{RT} = (kgA)^{-1/2}$ or RM external time scale $\tau_{RM} = (kA\Delta u)^{-1}$, (1.1) reduces accordingly to the RT-modified spectrum $E(k) = C_{RT}(gA)^{1/4}\varepsilon^{1/2}k^{-7/4}$ or RM-modified spectrum $E(k) = C_{RM}[A\Delta u\varepsilon]^{1/2}k^{-3/2}$. Here, g and A are the gravitational acceleration and the Atwood number, respectively, and Δu is the velocity jump induced by the shock wave. The power law of RM turbulence is still an open question. Some experimental (Weber *et al.* 2012; Reese *et al.* 2018) and numerical (Hill, Pantano & Pullin 2006; Lombardini, Pullin & Meiron 2012) studies found the Kolmogorov $-5/3$ power law, while other simulations obtained the $-3/2$ power law (Thornber *et al.* 2010; Tritschler *et al.* 2014*a*; Wong, Livescu & Lele 2019) or a shallower one (Cohen *et al.* 2002; Grinstein, Gowardhan

& Wachtor 2011). Compared with the energy spectrum, the structure function of RM turbulence has received less attention, except for few experimental works. Vorobieff, Rightley & Benjamin (1998) and Vorobieff *et al.* (2003) obtained a rough $2/3$ scaling of the second-order structure function in experiments. Also, Mohaghar *et al.* (2017) found this scaling for the structure function of RM turbulence after reshock. A scaling law with a steeper exponent than $2/3$ was found for the second-order structure functions of intensity maps by Olmstead *et al.* (2017), which was interpreted as the result of non-fully developed turbulence. Tomkins *et al.* (2013) obtained an even steeper scaling of the second-order density structure function in a gas-curtain experiment, which is attributed to the inertial range just beginning to form. Recently, Noble *et al.* (2020) found an anomalous scaling-law behaviour of the scalar structure function in their reshock experiments with small Schmidt number. So far, a phenomenological theory for the structure function of RM turbulence, which reveals more fluctuation information than the energy spectrum, has not yet been established.

Numerical simulation is also a useful tool to examine the structure function of RM turbulence. Nevertheless, high-fidelity simulation of compressible turbulence involving discontinuities (e.g. shock wave and material interface) and complex smooth regions (e.g. turbulent fluctuations) remains a great challenge today. The major difficulty is that simultaneous handling of discontinuities and turbulent fluctuations poses two contradictory demands on the numerical scheme. On the one hand, a certain amount of dissipation should be introduced into the numerical scheme to suppress spurious oscillations at discontinuities. On the other hand, to accurately resolve turbulent structures with a broad range of scales, the numerical scheme should possess minimal dispersion and dissipation.

In this work, we shall first perform high-fidelity simulations of RM turbulence with a new optimized weighted compact nonlinear scheme (WCNS) that has minimum dispersion and adaptive dissipation. The reliable flow field obtained will allow us to analyse the scaling law of the structure function of RM turbulence. Then, a phenomenological theory for the structure function of RM turbulence is developed. The theory will be adopted to examine the spatial and temporal scaling laws of the structure functions of the velocity and scalar for RM turbulence found in simulation and also for illustrating the differences between RM turbulence, RT turbulence and homogeneous isotropic turbulence (HIT).

2. Numerical methods

Three-dimensional multi-component Navier–Stokes (N–S) equations are adopted to describe the RM flow. The governing equations in conservative form are expressed as

$$\frac{\partial \rho}{\partial t} + \boldsymbol{\nabla} \cdot (\rho \boldsymbol{u}) = 0, \tag{2.1}$$

$$\frac{\partial \rho \boldsymbol{u}}{\partial t} + \boldsymbol{\nabla} \cdot (\rho \boldsymbol{u} \otimes \boldsymbol{u} + p\boldsymbol{\delta}) = \boldsymbol{\nabla} \cdot \boldsymbol{\sigma}, \tag{2.2}$$

$$\frac{\partial \rho E}{\partial t} + \boldsymbol{\nabla} \cdot [(\rho E + p)\boldsymbol{u}] = \boldsymbol{\nabla} \cdot (\boldsymbol{\sigma} \cdot \boldsymbol{u} - \boldsymbol{q}_c - \boldsymbol{q}_d), \tag{2.3}$$

$$\frac{\partial \rho Y_l}{\partial t} + \boldsymbol{\nabla} \cdot (\rho Y_l \boldsymbol{u}) = -\boldsymbol{\nabla} \cdot \boldsymbol{J}_l \quad (l = 1, \ldots, N-1), \tag{2.4}$$

where ρ, $\boldsymbol{u} = [u, v, w]^t$, p and E refer to the density, velocity vector, pressure and total energy per unit mass of the mixture, respectively, and $\boldsymbol{\delta}$ is the Kronecker delta.

The equation of state is

$$E = \frac{p}{\rho(\gamma - 1)} + \frac{1}{2}\boldsymbol{u} \cdot \boldsymbol{u}, \tag{2.5}$$

where γ is the specific heat ratio of the mixture and is calculated by

$$\gamma = \frac{\sum \dfrac{Y_l \gamma_l}{M_l(\gamma_l - 1)}}{\sum \dfrac{Y_l}{M_l(\gamma_l - 1)}}, \tag{2.6}$$

with Y_l, γ_l and M_l being the mass fraction, specific heat ratio and molar mass of species l, respectively. In this work, two species, air and SF_6, are considered. In the simulations, $\gamma_1 = 1.4$ and $M_1 = 28.964$ g mol^{-1} are adopted for air, $\gamma_2 = 1.094$ and $M_2 = 146.055$ g mol^{-1} for SF_6. The viscous stress tensor $\boldsymbol{\sigma}$, the conductive heat flux $\boldsymbol{q}_c$ and the interspecies enthalpy flux $\boldsymbol{q}_d$ are defined as

$$\boldsymbol{\sigma} = \mu[\nabla \boldsymbol{u} + (\nabla \boldsymbol{u})^t] - \tfrac{2}{3}\mu \nabla \cdot \boldsymbol{u}\boldsymbol{\delta}, \tag{2.7}$$

$$\boldsymbol{q}_c = -\kappa \nabla T, \tag{2.8}$$

$$\boldsymbol{q}_d = \sum_{k=1}^{N} c_{p,k} T \boldsymbol{J}_k. \tag{2.9}$$

Here, $c_{p,k}$ is the specific heat of species k at constant pressure, and the mass diffusion flux $\boldsymbol{J}_k$ is given by

$$\boldsymbol{J}_k = -\rho D_k \nabla Y_k \quad (k = 1, 2), \tag{2.10}$$

for binary mixture with $D_1 = D_2 = D_{12}$. The viscosity μ, the thermal conductivity κ and the mass diffusion coefficient D_{12} are calculated according to Tritschler *et al.* (2014*a*).

High-fidelity simulation of compressible turbulence involving discontinuities (e.g. shock wave and material interface) and turbulent fluctuations poses a great challenge to the numerical scheme. The major difficulty lies in the simultaneous capture of discontinuities and turbulent fluctuations. On the one hand, a certain amount of numerical dissipation should be introduced into the numerical scheme to suppress spurious oscillations at discontinuities. On the other hand, minimal dissipation and dispersion (i.e. good spectral properties) are needed to accurately resolve turbulent structures covering a broad range of scales. Previous studies have shown that the existing shock-capturing schemes such as the weighted essentially non-oscillatory (WENO) scheme (Jiang & Shu 1996) and the WCNS scheme (Deng & Zhang 2000) are too dissipative to resolve small-scale turbulence. The excessive dissipation of shock-capturing schemes comes from two sources: (i) the dissipation introduced by the nonlinear mechanism and (ii) the dissipation inherent in the linear part of a nonlinear scheme. Accordingly, there are two strategies to improve the dissipation property of shock-capturing schemes. One strategy is to optimize the nonlinear weighting function, which has a significant influence on the dissipation property of the nonlinear scheme. Recently, Wong & Lele (2017) presented a localized dissipation WCNS with improved nonlinear weights, which has been successfully applied to RM turbulence with reshock (Wong *et al.* 2019, 2022). Another strategy is to improve the spectral property of the corresponding linear scheme. It was found by Tam & Webb (1993) that the spectral property of a nonlinear scheme can be modulated by adjusting the free parameters introduced to the scheme, based on which an optimization strategy with controllable

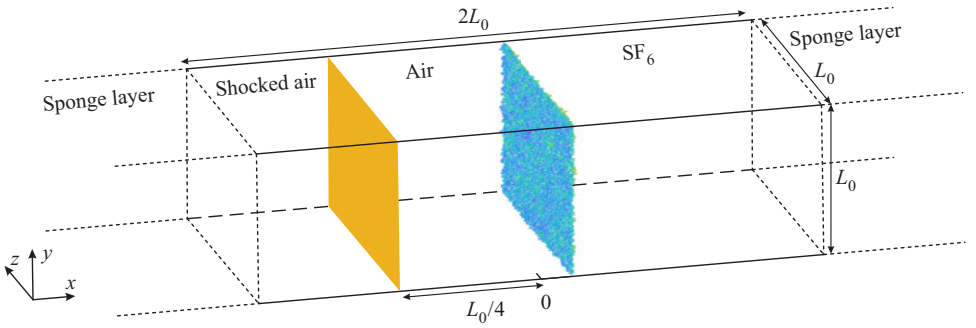

Figure 1. Schematic of the computational domain.

parameters was proposed (Sun *et al.* 2011). Although the free parameters reduce the formal order of accuracy of the scheme (i.e. the rate of convergence to the exact solution with grid refinement), they can significantly improve the scheme resolution (i.e. the actual truncation error on a given mesh).

Following this idea, we have recently proposed an adaptive, nonlinear optimization strategy that considers the diversity of flow structures and the influence of nonlinearity, based on which a new type of WCNS with state-of-the-art spectral properties was developed. The optimization procedure includes: (i) two free parameters in WCNS are optimized with the approximated dispersion relation technique (Pirozzoli 2006) that can attain the spectral properties of nonlinear WCNS; (ii) considering the nonlinear mechanism has a dramatic influence on the spectral properties, an advanced nonlinear weighting function of Wong & Lele (2017) is adopted and the crucial parameter, C, is optimized for better spectral properties; (iii) the optimized parameters are adjusted at each grid point according to the flow conditions there to realize adaptive dissipation. The optimized WCNS is extended to multi-species flows by combining the double-flux algorithm of Abgrall & Karni (2001) and is thus suitable for the simulation of RM turbulence. Note that the double-flux algorithm is not a conservative numerical method. As analysed by Abgrall & Karni (2001), there are the two main sources of conservation error for the double-flux algorithm, which have opposite effects on the solution and can nearly cancel each other out. As a result, it introduces only a little loss of conservation and thus produces a negligibly weak influence on the motions of shock and interface. In our previous work (Ding *et al.* 2017, 2018; Feng *et al.* 2021; Li *et al.* 2022), the double-flux algorithm combined with the fifth-order WENO scheme has shown the capacity of reproducing the experimental results for various RM instability flows. For more details about the present numerical scheme, readers are referred to Zhou *et al.* (2023).

As sketched in figure 1, the computational domain has a size of $2L_0 \times L_0 \times L_0$ ($L_0 =$ 10 mm) in the x, y and z directions, which is discretized by a Cartesian mesh with $1024 \times 512 \times 512$ grid points. Two long sponge layers with a stretched mesh are set at the left and right ends of the domain along the x direction, which can largely eliminate the influence of reflected waves. A periodic boundary condition is taken for the boundaries parallel to the x direction. A multi-mode interface between air and SF_6 at $p = 101\,325$ Pa and $T =$ 298.15 K is set at the beginning, whose average position is at $x = 0.11L_0$. A planar shock of $Ma = 1.5$ is initially set at $x = -L_0/4$ in air. To ensure the shocked interface evolves at the centre of the domain, the pre-shock gases are set to move at $\Delta U = -158.38$ m s^{-1}.

The initial multi-mode interface is set according to Groom & Thornber (2020), which has a power spectrum

$$P(k) = \begin{cases} Ck^m, & k_{min} < k < k_{max}, \\ 0, & \text{otherwise}, \end{cases} \tag{2.11}$$

where $k = \sqrt{k_y^2 + k_z^2}$ is the radial wavenumber. In this work, two cases with $m = 0$ are simulated. One case has initial narrowband Fourier modes, namely, $k_n \in (24, 40)$ with $k_n = (L_0/2\pi)k$ (called case NB). The other case has initial broadband Fourier modes, namely, $k_n \in (2, 64)$ (called case BB). To reach the turbulent state faster, the total standard deviation of the perturbation is fixed at $\sigma = 0.5\lambda_{min}$ for both cases. In order to deposit more kinetic energy on the post-shock interface to feed the subsequent turbulence, the initial interface thickness is set to be a small value of $\lambda_{min}/4$ (Lombardini *et al.* 2012).

The dissipation scale η, also known as the Kolmogorov scale, is usually considered as the smallest characteristic scale in turbulence. Thus, a criterion for direct numerical simulation (DNS) is that the grid is fine enough such that the dissipation scale is resolved. It is found in practical simulations that this criterion can be relaxed somewhat, namely, the grid size is of the order of η rather than equal to η (Moin & Mahesh 1998). According to the finding of Moin & Mahesh (1998) that most of the dissipation in the channel flow occurs at scales greater than 15η, Li *et al.* (2019) argued that a grid resolution of around 10η is qualified for DNS. Liu & Xiao (2016) and Tritschler *et al.* (2014*b*) advocated the criterion of Yeung & Pope (1989), i.e. the dissipation becomes extremely small beyond $k\eta = 1.5$, and thus $k_{\Delta max}\eta \geqslant 1.5$ ($k_{\Delta max} = \pi/\Delta$ with Δ the grid size) can be used as a criterion for DNS. With these two criteria, the grid resolution of the present simulations is examined, as shown in figure 2(*a*) where η is calculated by the method of Tritschler *et al.* (2014*b*). The results indicate that both cases satisfy the criterion of Moin & Mahesh (1998), but cannot meet the criterion of Yeung & Pope (1989). Actually, the more restrictive latter criterion is more appropriate for DNS, particularly for the study of high-order statistics. It should be noted that the idea of using the Kolmogorov scale to represent the smallest scale of the flow is not justifiable, because the time-dependent RM flow is not always in a state of fully developed turbulence (Groom & Thornber 2019; Zhou *et al.* 2021). Also, the shock-capturing scheme that involves numerical dissipation can influence the accuracy in estimating the viscous dissipation rate, and can further affect the calculated Kolmogorov scale. The present analysis shows that the grid resolution of the current simulations is close to, rather than at, the level of DNS. Note that the Schmidt number of the present flow is $Sc \approx 1$, under which the Bachelor scale is almost the same as the Kolmogorov scale. Since the N–S equations are solved with a high-resolution numerical scheme in this work, the present simulations (without an explicit subgrid-scale model) are referred to as high-fidelity N–S simulations according to Zhou *et al.* (2021). A grid sensitivity study on the turbulence statistics is given in the Appendix to show the uncertainty of the simulation results.

To better characterize the flow, the evolutions of the turbulence Reynolds number (Re_L) and Taylor Reynolds number (Re_{λ_T}) are given in figure 2(*b*). The former is characterized by large eddies and the latter is related to small and intermediate scales. These two Reynolds numbers are calculated by (Pope 2000)

$$Re_L = \frac{\langle K \rangle_{yz}^2}{\langle \rho \rangle_{yz} \langle \varepsilon \rangle_{yz} \langle \nu \rangle_{yz}}, \tag{2.12}$$

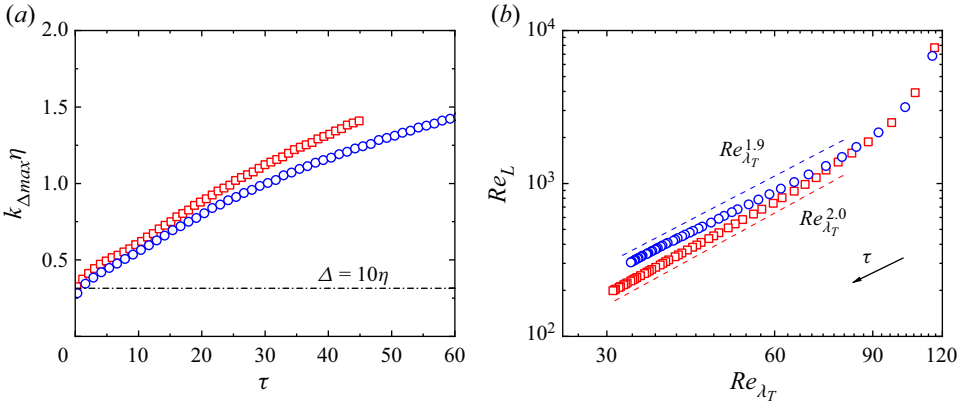

Figure 2. (*a*) Temporal evolution of the normalized Kolmogorov scale and (*b*) variation of the turbulence Reynolds number vs Taylor Reynolds number, averaged within the inner mixing zone, for case NB (squares) and case BB (circles).

and

$$Re_{\lambda_T} = \frac{\langle u_r'' \rangle_{yz} \langle \lambda_T \rangle_{yz}}{\langle \nu \rangle_{yz}}, \tag{2.13}$$

where $\langle K \rangle_{yz} = \sum_k E_{TKE}(k, x, t)$, $\varepsilon = \sum_k 2 \langle \nu \rangle_{yz} k^2 E_{TKE}(k, x, t)$ and $\nu = \mu/\rho$ are the kinetic energy, dissipation rate and kinematic viscosity, respectively; $u_r'' = (v''^2 + w''^2)^{1/2}$ and $\langle \lambda_T \rangle_{yz} = (10 \langle \nu \rangle_{yz} \langle K \rangle_{yz} / \langle \varepsilon \rangle_{yz})^{1/2}$ are the radial velocity fluctuation and Taylor scale, respectively; $\varphi'' = \varphi - \langle \rho\varphi \rangle_{yz} / \langle \rho \rangle_{yz}$ is defined as the fluctuating part of the Favre average, and $\langle \cdot \rangle_{yz}$ refers to the spatial average in the yz plane. The radial power spectrum for variable φ is given as

$$E_\varphi(k) = \sum_{k-1/2 < |\boldsymbol{k}_{yz}| \leqslant k+1/2} \hat{\varphi}^\star \hat{\varphi}, \tag{2.14}$$

where $\hat{\varphi}$ is the Fourier transform of φ in the yz plane, and $\hat{\varphi}^\star$ denotes its complex conjugate. In the present work, $\varphi = \sqrt{\rho} u_i''$ is used to calculate the spectrum of turbulent kinetic energy (TKE). As shown in figure 2(*b*), both cases present a similar evolution for Re_{λ_T} in the interval (30, 120) and for Re_L in the interval (200, 7000). The scaling for both cases is quite close to the relationship, $Re_L \propto Re_{\lambda_T}^2$, in HIT.

3. Characteristics of RM turbulence

The growth of the mixing width, which plays an important role in the establishment of the phenomenology for RM turbulence, is first investigated. The mixing width is calculated by

$$W_f = \int 4 \langle f_1 \rangle_{yz} \langle f_2 \rangle_{yz} \, \mathrm{d}x, \tag{3.1}$$

where f_1 and $f_2 = 1 - f_1$ denote the volume fractions of species 1 and 2, respectively. The mixing width is normalized as $W_f/\bar{\lambda}$ according to Groom & Thornber (2021). Here, $\bar{\lambda} = 2\pi/\bar{k} = L_0/\bar{k}_n$ is the average wavelength, in which $\bar{k}_n$ denotes the weighted average

wavenumber and is calculated by

$$\bar{k}_n = \frac{\sqrt{\int_0^\infty k^2 p(k)\,\mathrm{d}k}}{\sqrt{\int_0^\infty p(k)\,\mathrm{d}k}} = \sqrt{\frac{1}{3}\left(1+\frac{1}{R}+\frac{1}{R^2}\right)}k_{max}, \tag{3.2}$$

where $R = k_{max}/k_{min}$. Time is normalized by $\bar{\lambda}/\dot{W}_0$, where $\dot{W}_0$ is the initial growth rate that is estimated by

$$\dot{W}_0 = 0.564\bar{k}A^+\sigma_0^+\Delta U, \tag{3.3}$$

$$\sigma_0^+ = \left(1-\frac{\Delta U}{U_s}\right)\sigma_0, \tag{3.4}$$

where A^+ and σ^+ are the post-shock Atwood number and post-shock standard deviation of the perturbation, respectively, and U_s is the velocity of the initial shock.

As shown in figure 3(*a*), good agreement between the numerical result and the nonlinearly fitted curve is obtained, which indicates an evident $(\tau-\tau_0)^\theta$ (τ_0 is a virtual time origin) growth behaviour in the self-similar stage for each case. The curve fit is performed over the range $\tau \geqslant 5$ for both cases, and the fitted value of θ is 0.211 (0.333) for case NB (case BB). Recently, under the small Atwood number Boussinesq approximation, Soulard *et al.* (2018) deduced a relationship between the self-similar growth rate of the RM mixing layer and the infrared slope (s_0) of the post-shock velocity spectrum, $\theta = 2/(s_0+4)$, where $s_0 = m'+1$ with m' being the infrared exponent of the interface perturbation spectrum. According to Elbaz & Shvarts (2018) and Soulard *et al.* (2018), the evolution of the mixing width is influenced by both the behaviour of the large scale itself and the nonlinear backscatter of small scales to the large scale. For case NB with a high-wavenumber narrowband perturbation spectrum, the latter factor dominates the evolution of the mixing width. Based on this cognition, θ is predicted to be 1/3 by Elbaz & Shvarts (2018) and 1/4 by Soulard *et al.* (2018). For case BB with initial large-scale perturbations θ is expected to be 2/5 from the prediction of Soulard *et al.* (2018). Figure 3(*b*) gives the variation of the instantaneous growth rate exponent from simulation, which is calculated as $\theta = 1/(1+\beta)$ with $\beta = -W\ddot{W}/\dot{W}^2$ (Oggian *et al.* 2015). According to Oggian *et al.* (2015) and Groom & Thornber (2021), the fluctuations in θ are mainly ascribed to the numerical derivative (especially the second derivative) that magnifies the noise of the data. We state that this type of fluctuation does not hinder the judgment of the overall variation trend of θ. As we can see, the instantaneous value of θ is generally consistent with the fitted one. Moreover, it gradually approaches the prediction of Soulard *et al.* (2018) for each case. It is also seen that θ presents a trend of increasing to a higher value at the end time of the simulation.

Also, there are other definitions of the mixing width, such as the mass-fraction-based one, W_Y, which is calculated by replacing the volume fraction f with mass fraction Y in (3.1). The relationship between the two kinds of mixing width is investigated. Suggested by Boffetta *et al.* (2010), the integral length scale that represents the dynamical characteristic scale of large eddies is also investigated. Here, the integral length scale is calculated by

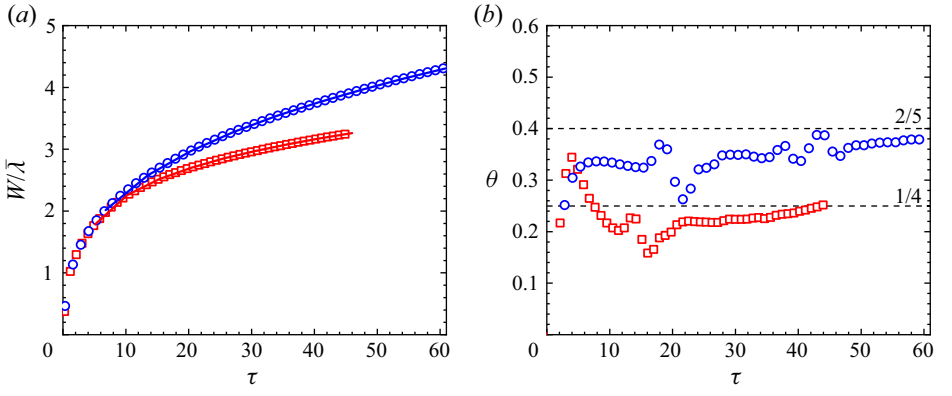

Figure 3. Temporal evolution of (*a*) the mixing width W and (*b*) the instantaneous growth rate exponent θ for case NB (squares) and case BB (circles). Lines in (*a*) represent the fit of $a(\tau - \tau_0)^\theta$, where τ_0 is a virtual time origin.

(Pope 2000)

$$\Lambda = \frac{3\pi}{4}\frac{\int_0^\infty E(k)/k\,\mathrm{d}k}{\int_0^\infty E(k)\,\mathrm{d}k}, \tag{3.5}$$

and then averaged in the inner mixing zone (IMZ) which is defined by $4Y(1-Y) \geqslant 0.9$ (Tritschler *et al.* 2014*a*). Figure 4 shows the variations of W_Y and Λ vs W_f. It is found that these scales are linearly related in the self-similar state. Performing a linear fit, the correlations of $W_Y \propto 1.01W_f$ ($W_Y \propto 1.17W_f$) and $\Lambda \propto 0.42W_f$ ($\Lambda \propto 0.36W_f$) for case NB (case BB) are obtained. This indicates that these typical large characteristic scales have similar scaling behaviour, which is favourable for the development of a phenomenological theory (Chertkov 2003).

Before moving to the discussion of the structure function, we examine the evolution of the IMZ-averaged TKE spectra calculated by (2.14) for cases NB and BB, as shown in figure 5. Since the dynamics of RM turbulence originates from the energy deposited by the initial shock wave, the initial perturbation spectrum at the interface determines the range of the energy scale (mainly in the direction of shock wave propagation). The Kolmogorov spectrum can only appear in the scale range below the initial maximum scale, and the spectrum above the initial maximum scale is mainly ascribed to the inverse transfer of energy from small to large scales.

For case NB with a high-wavenumber narrowband perturbation spectrum, there exists a visible $k^{-3/2}$ spectrum at the early stage. As time proceeds, the spectral peak shifts to lower wavenumbers and the $k^{-3/2}$ spectrum is gradually swallowed by a shallower spectrum, similar to the results of Tritschler *et al.* (2014*a*,*b*) and Grinstein *et al.* (2011). At the late stage, the range of the $k^{-3/2}$ spectrum becomes very narrow. We further examine the TKX (the x components of TKE) and TKYZ (the y and z components of TKE) spectra for case NB. Results show that the early spectral distributions in the x, y and z directions present significant differences. The x-component energy is higher than that of the y and z components, revealing the anisotropic characteristics of RM turbulence. The $k^{-3/2}$ spectrum of TKE at the early stage is mainly contributed by the x-component fluctuations. The yz-component only presents a narrower $k^{-3/2}$ spectrum at higher wavenumbers, which

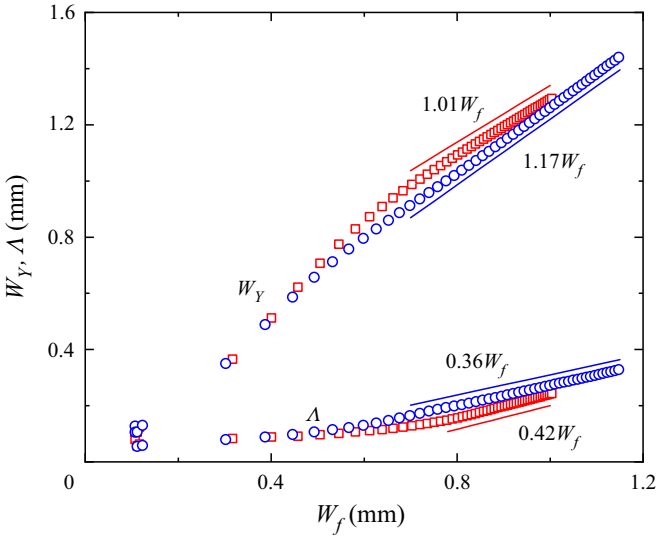

Figure 4. The variations of the mass-fraction-based mixing width W_Y and the integral length scale Λ vs the volume-fraction-based mixing width W_f. The symbols are the same as those in figure 3.

may be due to the energy transfer from the x direction to the yz-directions. For case BB with a broadband perturbation spectrum, at $\tau = 1.59$, the TKE, TKX and TKYZ show the $k^{(m+2)/2}$ spectrum ($m = 0$ in this work) suggested by Youngs (2004), which is consistent with the results of Groom & Thornber (2020). Later, a $k^{-3/2}$ spectrum appears for TKX, while TKYZ holds this spectrum in a narrower range at high wavenumbers. As time proceeds, the x-component gradually approaches the yz-component and the spectrum in the lower-wavenumber range becomes progressively shallower.

Figure 6 shows the spectra of Y_{SF_6} for both cases. As we can see, the mass fraction spectrum has a wider $k^{-3/2}$ spectral range than the TKE spectrum. This is more obvious in case BB.

Then, we consider the structure function of the longitudinal velocity, defined as $S_p^L(r, t) \equiv \left\langle |\delta_r u/u''_{rms}|^p \right\rangle$, where $\delta_r u = [\boldsymbol{u}(\boldsymbol{x} + \boldsymbol{r}, t) - \boldsymbol{u}(\boldsymbol{x}, t)] \cdot \hat{\boldsymbol{r}}$ with $\hat{\boldsymbol{r}} = \boldsymbol{r}/|\boldsymbol{r}|$ and u''_{rms} being the root-mean-square of the velocity fluctuation. Also, the scalar structure function in terms of the mass fraction of heavy fluid is examined, which is defined as $S_p^{Y_{SF_6}}(r, t) \equiv \left\langle |\delta_r Y_{SF_6}|^p \right\rangle$ where $\delta_r Y_{SF_6} = Y_{SF_6}(\boldsymbol{x} + \boldsymbol{r}, t) - Y_{SF_6}(\boldsymbol{x}, t)$. In this work, both velocity and scalar structure functions are calculated in a statistically homogeneous direction (e.g. the y direction) and then spatially averaged in the IMZ. Thus, $\boldsymbol{r}$ and $\langle\cdot\rangle$ in the above formulae can be replaced by $\boldsymbol{r_y} = (0, r_y, 0)$ and $\langle\cdot\rangle_{IMZ}$, respectively. We note that, whether $\boldsymbol{r_z} = (0, 0, r_z)$ or is averaged in the central plane of the mixing layer (Walchli & Thornber 2017), the main results are almost the same. Due to the limited computational resource, the turbulence simulated usually involves only a narrow inertial range, which increases the measurement uncertainty of the scaling exponent. To overcome this difficulty, an extended self-similarity (ESS) method (Benzi *et al.* 1995) that investigates the scaling of the nth-order structure function against the mth-order, i.e. $S_n(r) \sim S_m(r)^{\beta_{(n,m)}}$, is adopted to obtain an accurate relative scaling exponent, $\beta_{(n,m)} = \zeta_n/\zeta_m$. As suggested by Boffetta *et al.* (2010), here, the reference exponents for the structure functions of velocity and mass fraction take the forms

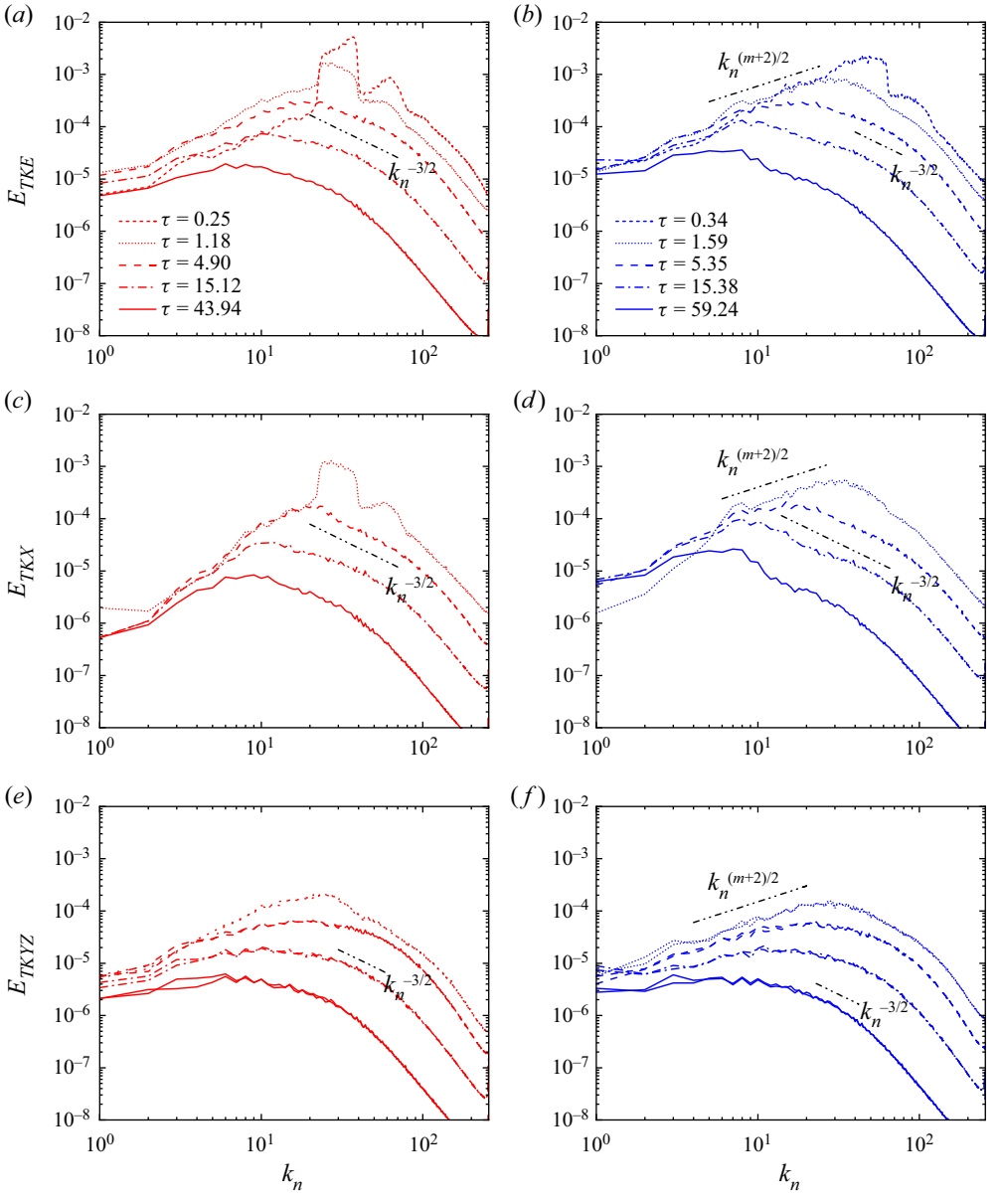

Figure 5. The TKE spectra (*a*,*b*), TKX spectra (*c*,*d*) and TKYZ spectra (*e*,*f*) of case NB (*a*,*c*,*e*) and case BB (*b*,*d*,*f*) at several times.

ζ_3^L and $\zeta_2^{Y_{SF_6}}$, respectively. Variations of the first- to sixth-order structure functions vs the reference one at a fixed time using a log–log scale for cases BB and NB are plotted in figure 7. As we can see, all orders of structure functions show a linear relationship with the reference one, which indicates the existence of ESS scaling. The slope of each-order structure function against the reference one corresponds to the relative scaling exponent. The values of $\beta_{(p,3)}^L$ and $\beta_{(p,2)}^{Y_{SF_6}}$ can be obtained via least-square fits. As shown in figure 7, the fitted lines agree well with the simulation results. It is also found that the scaling range

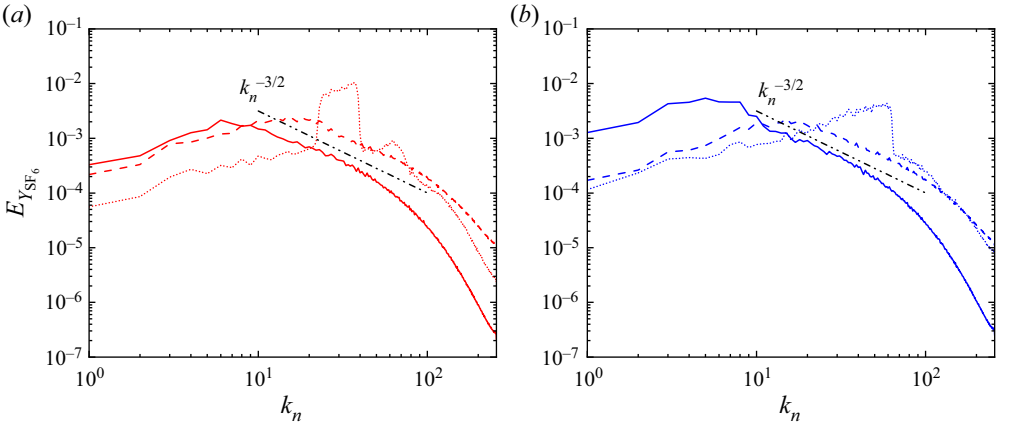

Figure 6. The radial spectra of mass fraction Y_{SF_6} for case NB (*a*) and case BB (*b*) at several times. The line styles represent the same times as in figure 5.

becomes narrower as p increases. Note that the fittings are carried out with an appropriate range of data points, which ensures that the distributions of the compensated structure functions against the reference one are as close as possible to the horizontal line (Pan & Scannapieco 2011), as shown in the insets of figure 7.

The relative scaling exponents obtained via least-square fits are given in figure 8, where the Kolmogorov–Obukhov–Corrsin (KOC) predictions are also given for comparison. Figure 8(*a*) also gives the relative scaling exponents in HIT with scalar injection by the Gaussian random source (Gotoh *et al.* 2011) and in RT turbulence at small Atwood number (Boffetta *et al.* 2010) for comparison. It is found that the relative exponents for RT turbulence and HIT are nearly identical to the present results of RM turbulence up to fourth order. At higher orders, there exists a visible discrepancy among them. The phenomenological theory fails to give an accurate prediction for $p > 3$, which indicates the existence of intermittency in the velocity field. This is a consequence of the breakdown of scale independence (an underlying assumption for phenomenological theory) caused by the fluctuations of energy and scalar dissipation rate. The relative scaling exponents for different types of turbulence are consistent with the prediction of the She–Leveque (SL) model (She & Leveque 1994) that considers the influence of intermittency. The present results give strong evidence that there exists intermittency for RM turbulence as with RT turbulence and HIT. Figure 8(*b*) gives a comparison of the scalar scaling exponent among the RM turbulence, RT turbulence, two types of HIT and the KOC prediction. Visible differences between the results of the two cases is observed. As we know, the 4/5 law by Kolmogorov (1941*a*) is related to the third-order structure function of the velocity, and the corresponding law by Obukhov (1949) and Corrsin (1951) is related to the second-order structure function passive scalar. This is the reason for the choices of $\beta^L_{(p,3)}$ for the velocity and $\beta^C_{(p,2)}$ for the scalar (Boffetta *et al.* 2010) here. It is found that the scalar scaling exponents for case NB nearly coincide with those of HIT with scalar injection through a uniform gradient, whereas the exponents for case BB coincide with those of RT turbulence and HIT with random Gaussian source. We note that the fluctuations in case NB are only generated by small-scale perturbations, while those in case BB are also related to the cascade of large-scale perturbations. The previous study of Gotoh *et al.* (2011) on HIT showed that the passive scalar fluctuations are excited at all scales for the case with scalar

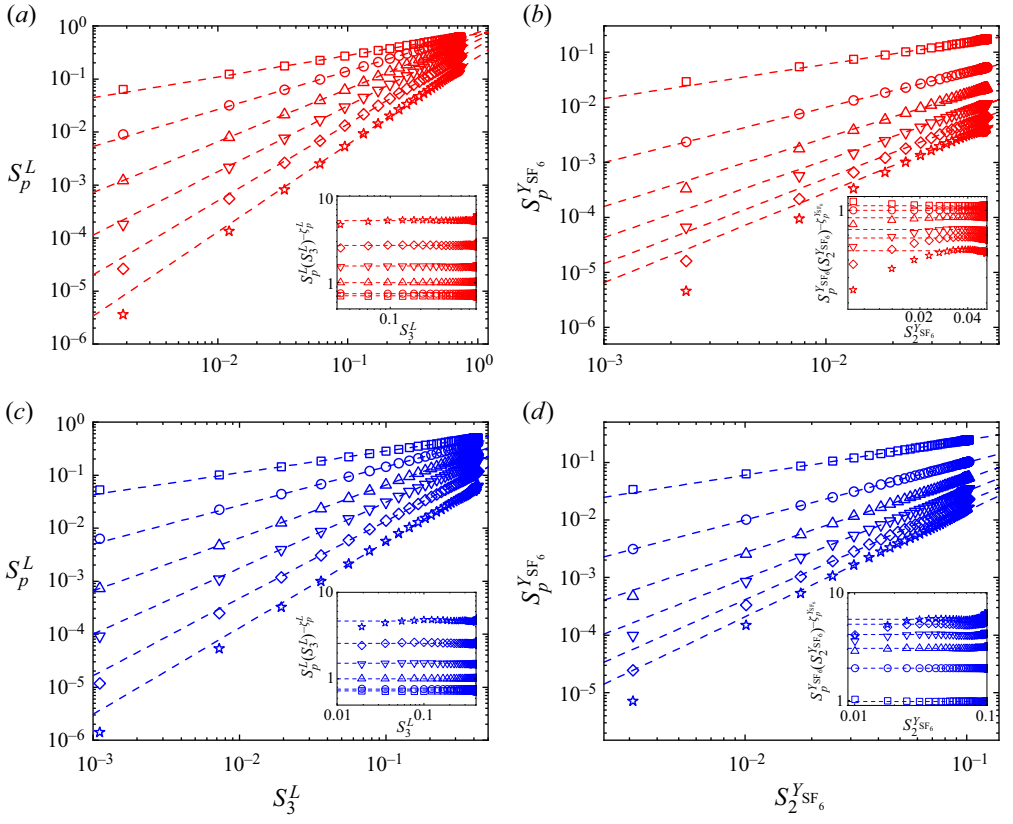

Figure 7. The ESS spatial scaling of (*a*,*c*) the longitudinal velocity structure function S_p^L and (*b*,*d*) the scalar structure function $S_p^{Y_{SF_6}}$ with $p = 1$ (squares), 2 (circles), 3 (up triangles), 4 (down triangles), 5 (diamonds), 6 (stars). Data are from (*a*,*b*) case NB at $\tau = 43.94$ and (*c*,*d*) case BB at $\tau = 59.24$. The insets are the corresponding compensated structure functions. Note that each plot of S_p^L is offset by 0.65, 0.35, 0.15 and 0.05 for $p = 3{-}6$, respectively. The plot of the compensated structure function in the inset of (*d*) is offset by p for $p = 2$–6, respectively.

injection by velocity excitation through a uniform gradient, but are mainly excited through the scale cascade for the case with scalar injection by a Gaussian random source at large scales. This can be used to speculate on the origin of the difference in passive scalar statistics at small scales under different initial conditions.

All simulation results deviate from the model prediction for $p > 2$, which is ascribed to the presence of intermittency. To support this statement, we undertake a hierarchical symmetry analysis that was originally proposed by She & Leveque (1994) and then rewritten by She *et al.* (2001):

$$\frac{F_{p+1}(r)}{F_2(r)} = \frac{A_p}{A_1}\left(\frac{F_p(r)}{F_1(r)}\right)^{\hat{\beta}}, \tag{3.6}$$

where $F_p(r) = S_{p+1}(r)/S_p(r)$ is the hierarchy, A_p is a parameter independent of r and $\hat{\beta} \leqslant 1$ reflects the degree of intermittency (lower value of $\hat{\beta}$ corresponds to stronger intermittency). It is noted that $\hat{\beta} = 1$ corresponds to the Kolmogorov scenario without intermittency, and $\hat{\beta} = (2/3)^{1/3} \approx 0.874$ in the SL model for isotropic turbulence.

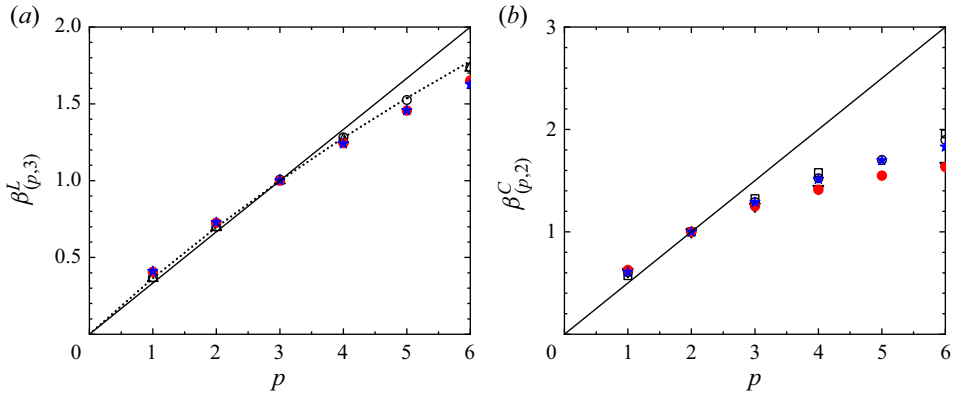

Figure 8. Relative scaling exponents for (*a*) longitudinal velocity structure functions $\beta^L_{(p,3)}$ and (*b*) scalar structure functions $\beta^C_{(p,2)}$. Data shown are from case NB (red filled circles), case BB (blue filled stars), DNS of RT turbulence with end time $Re_\lambda = 196$ in Boffetta *et al.* (2010) (black open circles), DNS of HIT with scalar injection by isotropic Gaussian random source at $Re_\lambda = 688$ (black up triangles) and by uniform gradient at $Re_\lambda = 586$ (black down triangles) in Gotoh, Watanabe & Suzuki (2011) and DNS of HIT with scalar injection by an isotropic random Gaussian source at $Re_\lambda = 427$ in Watanabe & Gotoh (2004) (black squares). Solid lines in both panels represent the KOC phenomenological predictions. The dotted line indicates the prediction of the She–Leveque model (She & Leveque 1994).

As shown in figure 9, the scaling of hierarchical symmetry with $\hat{\beta} < 1$ is obtained for the velocity and scalar in cases NB and case BB, which is consistent with the departures of the scaling exponents of the two cases from the KOC formulation. The value of $\hat{\beta} \approx 0.76$ for velocity is lower than the value used in the SL model, which explains the departures of the high-order scaling exponents of both cases from the prediction of the SL model. The lower value of $\hat{\beta}$ for scalar ($\approx$0.63) than that of velocity ($\approx$0.76) also corresponds to the stronger intermittency of the scalar than the velocity. The present analysis indicates that intermittency is closely related to the symmetry breaking between scales. As we know, the symmetry breaking is related to a variety of factors such as the flow type, initial conditions, Mach number and so on. This may be the reason why cases BB and NB with different initial perturbation spectra present different degrees of intermittency.

From the present results, two claims can be made for RM turbulence. First, as we know, the only difference between case NB and case BB is the initial perturbation spectrum. Since these two cases present different behaviours of small-scale statistics, it is reasonable to speculate that larges scales in case BB can influence the statistics of small scales. Especially, it is found that the difference in anomalous scaling exponents between case NB and case BB is larger for the scalar structure function than the velocity structure function. This indicates that the statistics of small-scale scalar fluctuations suffer a larger influence of large scales than the velocity fluctuation. Second, the scalar field exhibits a greater degree of intermittency than the velocity field under the current Mach number. Particularly, the deviation of the RM turbulence from other types of turbulence for both β^L_p and β^C_p highlights the unique characteristic of RM turbulence, and thus a specific phenomenological theory for RM turbulence is desired.

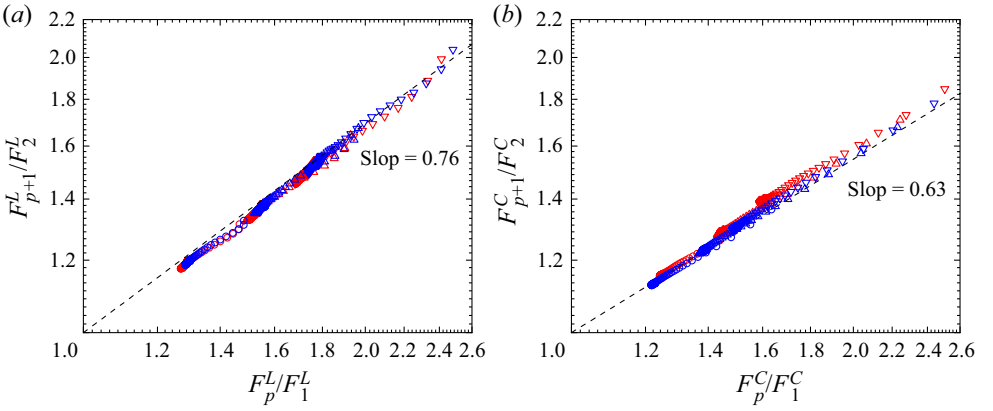

Figure 9. Scaling of hierarchical symmetry of (*a*) velocity and (*b*) scalar for case NB (red) and case BB (blue) with $p = 2$ (circles), 3 (up triangles) and 4 (down triangles).

4. Phenomenological model and validation

A key idea of the present phenomenological theory for RM turbulence is to introduce an external agent inspired by Zhou (2001). With (1.1) and the definition $\varepsilon = U^2(k)/\tau_s(k)$, we have the spectral transfer time $\tau_s(k) = [\tau_{eddy}(k)]^2/[C_\tau^2\tau_{tr}(k)]$. Assuming the kinetic energy flux $\varepsilon(t)$ is scale independent in the inertial range, we get

$$\delta_r u(t) \sim \varepsilon(t)^{1/2}[\tau_s(k_r)]^{1/2} \sim u_L(t)[r/L(t)]^{1/2}[\tau_{tr}(k_L)/\tau_{tr}(k_r)]^{1/4}. \tag{4.1}$$

Without an external agent, $\tau_{tr}(k)$ can be represented by the eddy-turnover time scale $\tau_{eddy}(k_r) = r/u_r \sim r/\delta_r u$, producing a scaling law $\delta_r u(t) \sim u_L(t)[r/L(t)]^{1/3}$. This is exactly equal to that of Chertkov (2003). If an external agent exists, the time scale is treated in a way similar to Zhou (2001). Specifically, for RT turbulence, $\tau_{tr}(k)$ in (4.1) is substituted by τ_{RT}, producing a scaling law $\delta_r u(t) \sim u_L(t)[r/L(t)]^{3/8}$. For RM turbulence, $\tau_{tr}(k) = \tau_{RM}$, producing a scaling law $\delta_r u(t) \sim u_L(t)[r/L(t)]^{1/4}$. As has been pointed out by Pope (2000), if the inertial range presents a k^{-n} energy spectrum, its second-order structure function should follow a r^{ζ_2} scaling law with $\zeta_2 = \min(n-1, 2)$. Based on this rule, the scaling laws of the structure functions derived here correspond to the $k^{-5/3}$ Kolmogorov spectrum, the $k^{-7/4}$ RT spectrum and the $k^{-3/2}$ RM spectrum, which are the same as those of Zhou (2001). This demonstrates the validity of the present phenomenological theory.

Compared with the velocity field, the scalar field possesses a more complex spectrum that is dependent on the Schmidt number *Sc* (Sreenivasan 2019). In this work, to facilitate the derivation of a phenomenological model for the scalar, we consider a fundamental yet important case with two constraints: the mechanisms of velocity fluctuation and scalar fluctuation are the same; $Sc = O(1)$. With these constraints, the inertial range of the velocity field nearly matches that of the scalar field, and also their time scales are equal (Gotoh & Yeung 2012). Assuming the scalar variance flux $\varepsilon_C(t)$ is scale independent in the inertial–convective range, following a procedure similar to that of the velocity field, we get

$$\delta_r C(t) \sim \varepsilon_C(t)^{1/2}[\tau_s(k_r)]^{1/2} \sim \Delta C[r/L(t)]^{1/2}[\tau_{tr}(k_L)/\tau_{tr}(k_r)]^{1/4}. \tag{4.2}$$

Similarly, in (4.2), $\tau_{tr} = \tau_{eddy}$ leads to $\delta_r C(t) \sim \Delta C[r/L(t)]^{1/3}$ for the Obukhov–Corrsin scenario, $\tau_{tr} = \tau_{RT}$ to $\delta_r C(t) \sim \Delta C[r/L(t)]^{3/8}$ for RT turbulence and $\tau_{tr} = \tau_{RM}$ to $\delta_r C(t) \sim \Delta C[r/L(t)]^{1/4}$ for RM turbulence.

The spatial scaling laws described by (4.1) and (4.2) are independent of $L(t)$. By introducing a self-similar growth $L(t) \sim t^{\theta}$, temporal scaling laws for the structure functions of velocity and scalar are obtained:

$$\left\langle (\delta_r u)^p \right\rangle \sim u_L(t)^p \left[\frac{r}{L(t)}\right]^{\zeta_p} \sim r^{\zeta_p} t^{(\theta-1)p-\theta\zeta_p}, \tag{4.3}$$

$$\left\langle (\delta_r C)^p \right\rangle \sim (\Delta C)^p \left[\frac{r}{L(t)}\right]^{\zeta_p^C} \sim r^{\zeta_p^C} t^{-\theta\zeta_p^C}, \tag{4.4}$$

where ζ_p and ζ_p^C are the spatial scaling exponents of the pth-order structure functions of velocity and scalar increments, respectively. As found above, $\zeta_p = \zeta_p^C = p/3$ for the classical KOC scenario, $\zeta_p = \zeta_p^C = 3p/8$ for RT turbulence and $\zeta_p = \zeta_p^C = p/4$ for RM turbulence. Equations (4.3) and (4.4) indicate that the temporal scaling exponents are closely related to the spatial scaling exponents as well as the scaling law of mixing width. To the authors' knowledge, this is the first time the spatial and temporal scaling laws of the structure functions for RM turbulence have been given.

With the relative scaling exponents in figure 8, we can calculate the absolute scaling exponents. The distributions of S_p^L vs the spatial scale r_y at $\tau = 59.24$ for case BB are given in figure 10(*a*), where the prediction of the Kolmogorov scenario ($\zeta_p^L = p/3$) and the RM-modified anomalous exponents calculated from $\beta_{(p,3)}^L$ with a reference value of $\zeta_3^L = 3/4$ are also given for comparison. It is seen that the simulation results deviate from the Kolmogorov exponents, but are quite close to the RM-modified anomalous exponents in the short scaling range. This demonstrates the validity of the present phenomenological theory. Figure 10(*b*) gives the distributions of $\zeta_p^{Y_{SF_6}}$ vs the spatial scale, where the dimensional prediction of the Obukhov–Corrsin scenario ($\zeta_p^{Y_{SF_6}} = p/3$) and two anomalous exponents calculated from $\beta_{(p,2)}^{Y_{SF_6}}$ are given for comparison. Since $\zeta_2^C = 2/3$ is not an exact value for the Obukhov–Corrsin scenario, here $\zeta_2^C = 0.659$ from the DNS of HIT (Watanabe & Gotoh 2004) is taken as the reference exponent to obtain the Obukhov–Corrsin anomalous exponent. The reference value $\zeta_2^{Y_{SF_6}} = 0.659 \times 3/4$ is used to calculate the RM-modified anomalous exponent. As shown in figure 10(*b*), the simulation results deviate from the Obukhov–Corrsin scaling exponents, particularly for high-order structure functions. The values of $\zeta_p^{Y_{SF_6}}$ from simulation agree with the Obukhov–Corrsin anomalous scaling exponents at small scales, but approach the RM-modified anomalous ones at large scales. The present results reveal the influence of the external agent on the scaling laws of the structure functions for RM turbulence. The agreements between the simulation results and the model predictions for $\zeta_p^{Y_{SF_6}}$ also give a direct demonstration of the validity of the present phenomenological theory. Case NB presents similar results with a relative narrower scaling range, which are not shown here.

Finally, we investigate the temporal scaling behaviour of the structure functions of the longitudinal velocity and scalar. Figure 11 shows the ESS scaling of the structure functions against the reference one at a fixed spatial scale $r_0 = 15\Delta_{yz}$ for case BB. The fixed scale chosen here is located inside the scaling range in figure 10. Two prediction lines of the

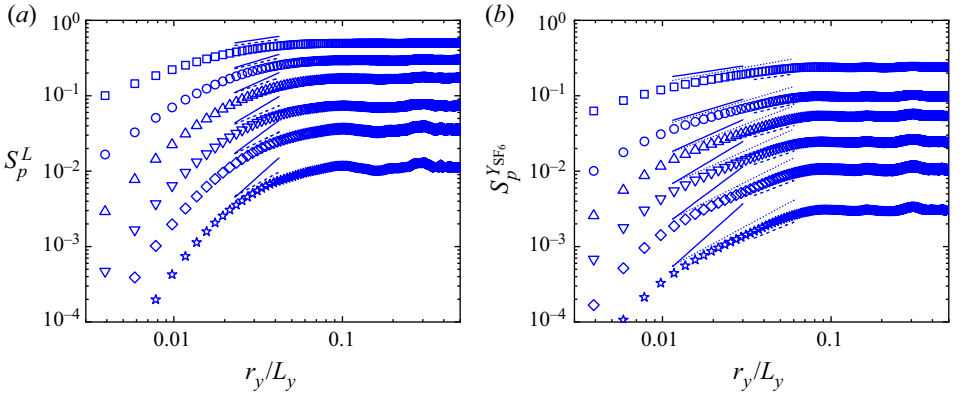

Figure 10. Spatial scaling of (*a*) longitudinal velocity structure function S_p^L and (*b*) scalar structure function $S_p^{Y_{SF_6}}$ at $\tau = 59.24$ for case BB. Note that the plot of S_p^L is offset by 0.75, 0.4, 0.15, 0.05 and 0.01 for $p = 2$–6, respectively; the plot of $S_p^{Y_{SF_6}}$ is offset by 0.8, 0.5 and 0.2 for $p = 4$–6, respectively. Here, symbols represent the same value of p as in figure 7. Sold lines in both panels represent the scaling exponents of the KOC phenomenological prediction. Dot lines and dash lines represent the KOC and RM-modified anomalous scaling exponents, respectively.

present phenomenological model for the KOC and RM-modified scenarios are given for comparison. The former uses the non-intermittent spatial scaling exponents while the latter adopts the anomalous ones used in figure 10. The fitted value of $\theta = 0.333$, which can represent the overall growth behaviour of the mixing width of case BB, is used for both lines. As shown in figure 11(*a*), the predicted exponents of $S_p^L(r_0, t)$ are not sensitive to ζ_p and both prediction lines are in good agreement with the simulation results at most times. As shown in figure 11(*b*), unlike the results of $S_p^L(r_0, t)$, the two prediction lines of $S_p^{Y_{SF_6}}(r_0, t)$ exhibit a distinct difference. The simulation results first meet the RM-modified anomalous scaling, and then approach the KOC non-intermittent scaling. It is found that the power-law range gradually shifts to large scales due to both the growth of the mixing zone and the decrease of the Reynolds number in RM turbulence, which is a possible reason for the switch in the ESS temporal scaling of the scalar.

5. Conclusions

In this work, high-fidelity simulations of RM turbulence with two different initial perturbation spectra (i.e. case BB and case NB) are performed with an improved WCNS scheme that has minimum dispersion and adaptive dissipation. The features of RM turbulence are first investigated. The mixing width experiences an exponential growth behaviour in the self-similar stage. The measured values of the exponent for both cases approach the predictions of Soulard *et al.* (2018). A visible $-3/2$ spectrum of the TKE is observed in RM turbulence, which confirms the prediction of Zhou (2001).

A phenomenological theory for the structure functions of the velocity and scalar of RM turbulence is developed by introducing an external agent originally proposed by Zhou (2001). Both simulation and theory show an evident influence of the external agent on the scaling laws of the inertial range for RM turbulence. The simulation results give strong evidence of intermittency for RM turbulence as with RT turbulence and HIT, and the relative scaling exponents for these types of turbulence obtained with the ESS method

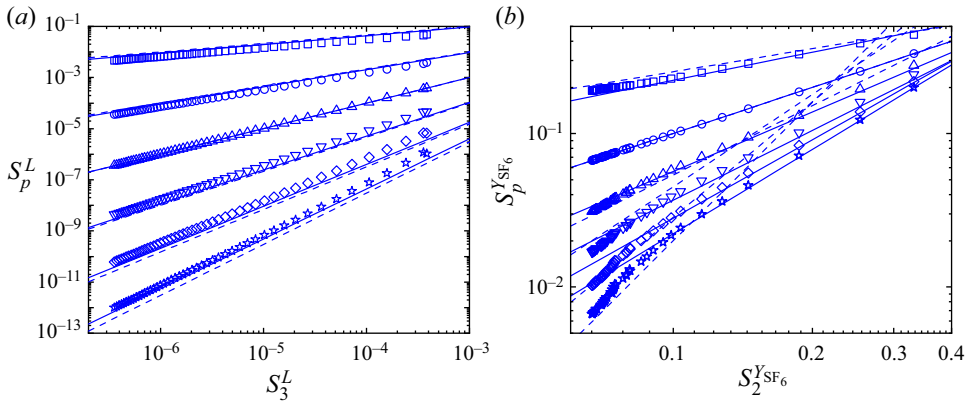

Figure 11. The ESS temporal scaling of (*a*) longitudinal velocity $S_p^L(r_0, t)$ and (*b*) scalar structure function $S_p^{Y_{SF_6}}(r_0, t)$ at fixed spatial scale for case BB. Dash lines and solid lines in both panels represent the predictions from phenomenological theory with the KOC non-intermittent and RM-modified anomalous spatial scaling exponents, respectively. Here, symbols represent the same value of p as in figure 7.

are generally consistent. For RM turbulence, the scalar field exhibits a greater degree of intermittency than the velocity field under the current Mach number. Also, the statistics of small-scale scalar fluctuations suffer a larger influence of large scales than the velocity fluctuation. A hierarchical symmetry analysis is undertaken, and the result indicates that intermittency is closely related to the symmetry breaking between scales. The spatial scaling exponents of the structure functions from simulation deviate from the Kolmogorov exponents, but are quite close to the RM-modified anomalous exponents in the short scaling range. The agreements between the simulation and prediction for the spatial scaling exponents of both the velocity and scalar structure functions give a direct demonstration of the validity of the present phenomenological theory. The temporal scaling exponents of the structure functions first meet the RM-modified anomalous scaling, and then approach the KOC non-intermittent scaling. In the future, RM turbulence at sufficiently high Reynolds numbers should be studied to address several key issues: explore the universal scenario; clarify whether the KOC theory is the only scenario in the limits of large Reynolds number, long times and small scales; construct a relationship between the change of scaling law and the mixing transition.

Funding. This work was supported by the National Natural Science Foundation of China (nos. 91952205, 12122213 and 12072341) and the National Key Research and Development Program of China (2022YFF0504500). The simulations were supported by the Supercomputing Center of University of Science and Technology of China (USTC).

Declaration of interests. The authors report no conflict of interest.

Author ORCIDs.
Juchun Ding https://orcid.org/0000-0001-6578-1694;
Wan Cheng https://orcid.org/0000-0003-3960-4162;
Xisheng Luo https://orcid.org/0000-0002-4303-8290.

Appendix

Figures 12(*a*,*b*) and 12(*c*,*d*) show the comparisons of TKE spectra and mass fraction spectra between the fine (1024 × 512 × 512) and coarse (512 × 256 × 256) meshes for

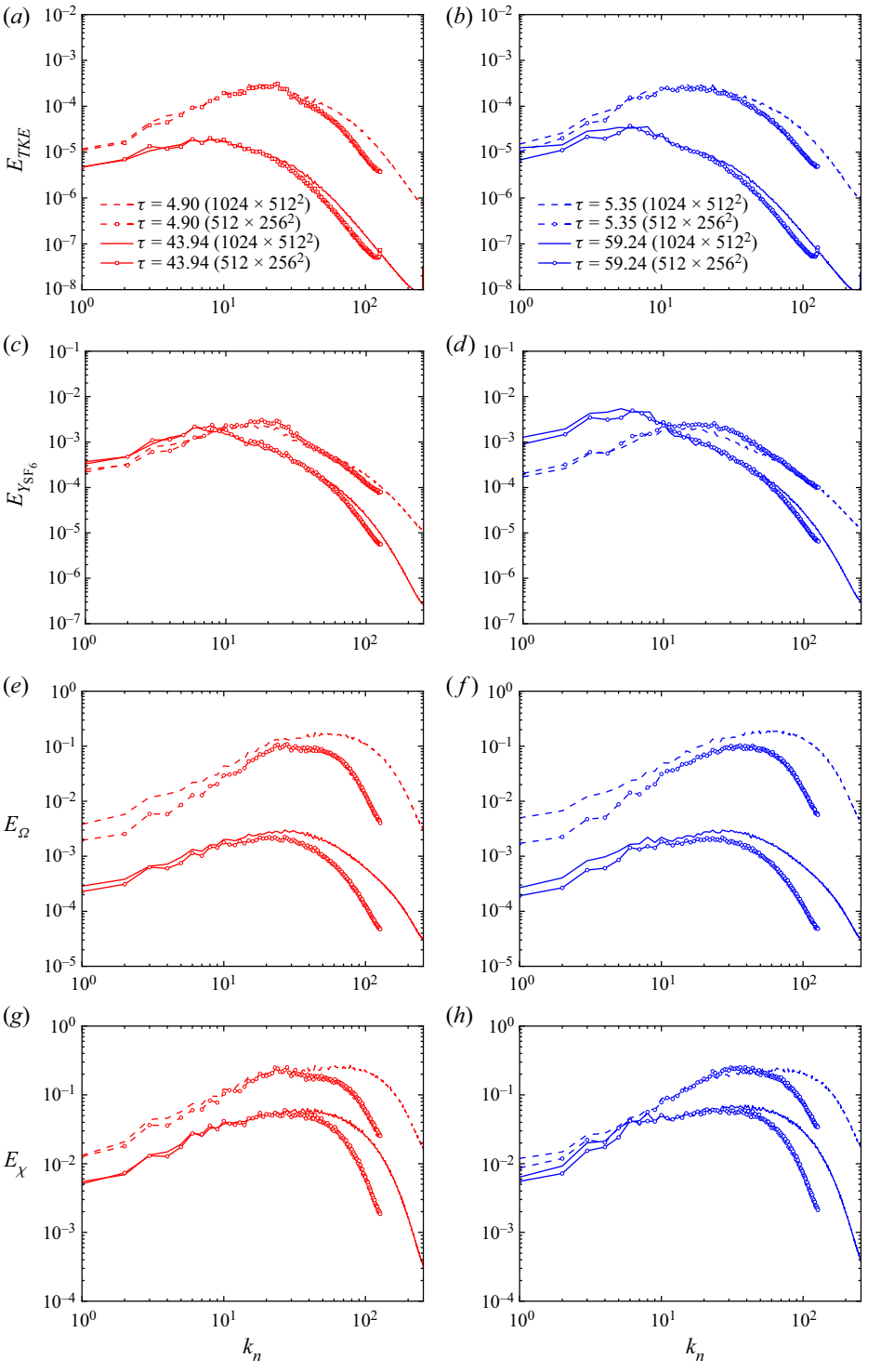

Figure 12. Spectra of TKE (*a*,*b*), mass fraction (*c*,*d*), enstrophy (*e*,*f*) and scalar dissipation rate (*g*,*h*) at two different times for case NB (*a*,*c*,*e*,*g*) and case BB (*b*,*d*,*f*,*h*) with grid numbers of 512 × 256 × 256 (lines with symbol) and 1024 × 512 × 512 (lines).

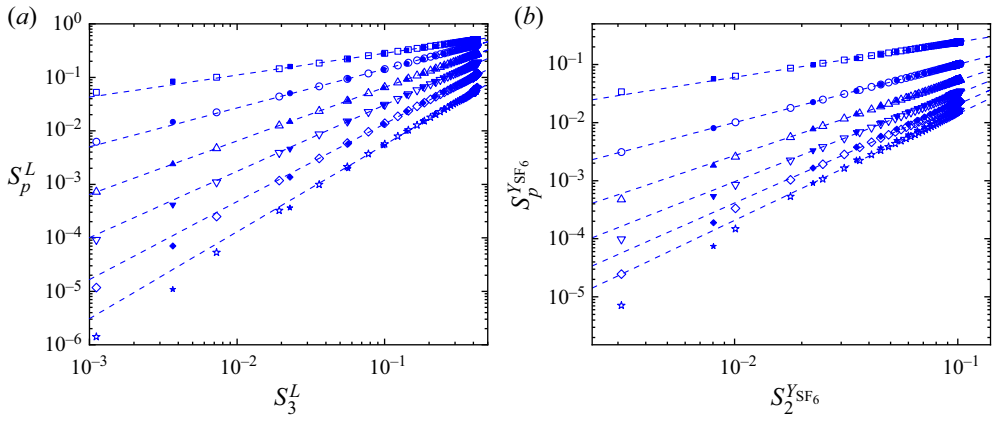

Figure 13. The ESS spatial scaling of (*a*) longitudinal velocity structure function S_p^L and (*b*) scalar structure function $S_p^{Y_{SF_6}}$ for case BB with grid numbers of 512 × 256 × 256 (solid symbols) and 1024 × 512 × 512 (open symbols). The symbols represent the same value of p as in figure 7.

cases NB and BB. As we can see, the spectra in the scaling range under the two meshes are quite close, while the spectrum at high wavenumbers is lower for the coarse mesh than the fine mesh due to the grid-dependent numerical dissipation. The spectra of enstrophy and scalar dissipation rate, which are more grid sensitive (Tritschler *et al.* 2014*b*; Groom & Thornber 2019), are given in figures 12(*e*,*f*) and 12(*g*,*h*), respectively. Reasonable agreement is obtained at low wavenumbers for the spectrum of the scalar dissipation rate for the fine and coarse meshes. The spectrum of enstrophy is found to be lower at all wavenumbers for the coarse mesh than for the fine mesh. The difference is explained below. In the present simulations, in order to deposit more kinetic energy on the interface to feed the subsequent turbulence, the initial interface thickness is set to be a small value of $\lambda_{min}/4$ (Lombardini *et al.* 2012). As a result, the initial interface is sharp for the coarser mesh, but presents a diffusive layer for the fine mesh. This accounts for the relatively large difference in the spectra of enstrophy.

To further examine the mesh sensitivity of the main results reported in this work, comparisons of the structure functions under the two meshes are given in figure 13. It is seen that the ESS scalings are in reasonable agreement for the two grid resolutions except for the minor difference at high orders. This manifests the reliability of the scaling exponents obtained from the present high-fidelity N–S simulations.

References

Abarzhi, S.I., Bhowmick, A.K., Naveh, A., Pandian, A., Swisher, N.C., Stellingwerf, R.F. & Arnett, W.D. 2019 Supernova, nuclear synthesis, fluid instabilities, and interfacial mixing. *Proc. Natl Acad. Sci. USA* **116** (37), 18184–18192.

Abgrall, R. & Karni, S. 2001 Computations of compressible multifluids. *J. Comput. Phys.* **169**, 594–623.

Benzi, R. & Biferale, L. 2015 Homogeneous and isotropic turbulence: a short survey on recent developments. *J. Stat. Phys.* **161**, 1351–1365.

Benzi, R., Ciliberto, S., Baudet, C. & Chavarria, G.R. 1995 On the scaling of three-dimensional homogeneous and isotropic turbulence. *Physica* D **80** (4), 385–398.

Boffetta, G., Mazzino, A., Musacchio, S. & Vozella, L. 2010 Statistics of mixing in three–dimensional Rayleigh–Taylor turbulence at low Atwood number and Prandtl number one. *Phys. Fluids* **22** (3), 035109.

CASNER, A. 2021 Recent progress in quantifying hydrodynamics instabilities and turbulence in inertial confinement fusion and high-energy-density experiments. *Phil. Trans. R. Soc. Lond.* A **379** (2189), 20200021.

CHERTKOV, M. 2003 Phenomenology of Rayleigh–Taylor turbulence. *Phys. Rev. Lett.* **91**, 115001.

COHEN, R.H., DANNEVIK, W.P., DIMITS, A.M., ELIASON, D.E., MIRIN, A.A., ZHOU, Y., PORTER, D.H. & WOODWARD, P.R. 2002 Three-dimensional simulation of a Richtmyer–Meshkov instability with a two-scale initial perturbation. *Phys. Fluids* **14** (10), 3692–3709.

CORRSIN, S. 1951 On the spectrum of isotropic temperature fluctuations in an isotropic turbulence. *J. Appl. Phys.* **22** (4), 469–473.

DENG, X.G. & ZHANG, H.X. 2000 Developing high-order weighted compact nonlinear schemes. *J. Comput. Phys.* **165** (1), 22–44.

DIMONTE, G., YOUNGS, D.L., DIMITS, A., WEBER, S., MARINAK, M., WUNSCH, S., GARASI, C., ROBINSON, A., ANDREWS, M.J., RAMAPRABHU, P., *et al.* 2004 A comparative study of the turbulent Rayleigh–Taylor instability using high-resolution three-dimensional numerical simulations: the Alpha-Group collaboration. *Phys. Fluids* **16** (5), 1668–1693.

DING, J., LIANG, Y., CHEN, M., ZHAI, Z., SI, T. & LUO, X. 2018 Interaction of planar shock wave with three-dimensional heavy cylindrical bubble. *Phys. Fluids* **30** (10), 106109.

DING, J., SI, T., CHEN, M., ZHAI, Z., LU, X. & LUO, X. 2017 On the interaction of a planar shock with a three-dimensional light gas cylinder. *J. Fluid Mech.* **828**, 289–317.

ELBAZ, Y. & SHVARTS, D. 2018 Modal model mean field self-similar solutions to the asymptotic evolution of Rayleigh–Taylor and Richtmyer–Meshkov instabilities and its dependence on the initial conditions. *Phys. Plasmas* **25** (6), 062126.

FENG, L., XU, J., ZHAI, Z. & LUO, X. 2021 Evolution of shock-accelerated double-layer gas cylinder. *Phys. Fluids* **33** (8), 086105.

GOTOH, T., WATANABE, T. & SUZUKI, Y. 2011 Universality and anisotropy in passive scalar fluctuations in turbulence with uniform mean gradient. *J. Turbul.* **12**, N48.

GOTOH, T. & YEUNG, P.K. 2012 *Passive Scalar Transport in Turbulence: A Computational Perspective*, pp. 87–131. Cambridge University Press.

GRINSTEIN, F.F., GOWARDHAN, A.A. & WACHTOR, A.J. 2011 Simulations of Richtmyer–Meshkov instabilities in planar shock-tube experiments. *Phys. Fluids* **23** (3), 2931.

GROOM, M. & THORNBER, B. 2019 Direct numerical simulation of the multimode narrowband Richtmyer–Meshkov instability. *Comput. Fluids* **194**, 104309.

GROOM, M. & THORNBER, B. 2020 The influence of initial perturbation power spectra on the growth of a turbulent mixing layer induced by Richtmyer–Meshkov instability. *Physica* D **407**, 132463.

GROOM, M. & THORNBER, B. 2021 Reynolds number dependence of turbulence induced by the Richtmyer–Meshkov instability using direct numerical simulations. *J. Fluid Mech.* **908**, A31.

HILL, D.J., PANTANO, C. & PULLIN, D.I. 2006 Large-eddy simulation and multiscale modelling of a Richtmyer–Meshkov instability with reshock. *J. Fluid Mech.* **557**, 29–61.

JIANG, G.S. & SHU, C.W. 1996 Efficient implementation of weighted ENO schemes. *J. Comput. Phys.* **126** (1), 202–228.

KOLMOGOROV, A.N. 1941*a* Dissipation of energy in locally isotropic turbulence. *Dokl. Akad. Nauk SSSR* **32**, 16.

KOLMOGOROV, A.N. 1941*b* The local structure of turbulence in incompressible viscous fluid for very large Reynolds numbers. *Dokl. Akad. Nauk SSSR* **30**, 301–305.

LI, H., HE, Z., ZHANG, Y. & TIAN, B. 2019 On the role of rarefaction/compression waves in Richtmyer–Meshkov instability with reshock. *Phys. Fluids* **31** (5), 054102.

LI, J., DING, J., LUO, X. & ZOU, L. 2022 Instability of a heavy gas layer induced by a cylindrical convergent shock. *Phys. Fluids* **34** (4), 042123.

LIU, H. & XIAO, Z. 2016 Scale-to-scale energy transfer in mixing flow induced by the Richtmyer–Meshkov instability. *Phys. Rev.* E **93**, 053112.

LOMBARDINI, M., PULLIN, D.I. & MEIRON, D.I. 2012 Transition to turbulence in shock-driven mixing: a Mach number study. *J. Fluid Mech.* **690**, 203–226.

MESHKOV, E.E. 1969 Instability of the interface of two gases accelerated by a shock wave. *Fluid Dyn.* **4**, 101–104.

MIKAELIAN, K.O. 1989 Turbulent mixing generated by Rayleigh–Taylor and Richtmyer–Meshkov instabilities. *Physica* D **36**, 343–357.

MOHAGHAR, M., CARTER, J., MUSCI, B., REILLY, D., MCFARLAND, J. & RANJAN, D. 2017 Evaluation of turbulent mixing transition in a shock-driven variable-density flow. *J. Fluid Mech.* **831**, 779–825.

MOHAGHAR, M., CARTER, J., PATHIKONDA, G. & RANJAN, D. 2019 The transition to turbulence in shock-driven mixing: effects of mach number and initial conditions. *J. Fluid Mech.* **871**, 595–635.

MOIN, P. & MAHESH, K. 1998 Direct numerical simulation: a tool in turbulence research. *Annu. Rev. Fluid Mech.* **30** (1), 539–578.

NOBLE, C.D., HERZOG, J.M., ROTHAMER, D.A., AMES, A.M., OAKLEY, J. & BONAZZA, R. 2020 Scalar power spectra and scalar structure function evolution in the Richtmyer–Meshkov instability upon reshock. *Trans. ASME J. Fluids Engng* **142** (12), 121102.

OBUKHOV, A.M. 1949 Structure of the temperature field in turbulent flows. *Izv. Acad. Nauk SSSR Geogr. Geofiz* **13**, 58–69.

OGGIAN, T., DRIKAKIS, D., YOUNGS, D.L. & WILLIAMS, R.J.R. 2015 Computing multi–mode shock-induced compressible turbulent mixing at late times. *J. Fluid Mech.* **779**, 411–431.

OLMSTEAD, D., WAYNE, P., SIMONS, D., TRUEBA MONJE, I., YOO, J.H., KUMAR, S., TRUMAN, C.R. & VOROBIEFF, P. 2017 Shock-driven transition to turbulence: emergence of power-law scaling. *Phys. Rev. Fluids* **2**, 052601.

PAN, L. & SCANNAPIECO, E. 2011 Passive scalar structures in supersonic turbulence. *Phys. Rev.* E **83**, 045302.

PIROZZOLI, S. 2006 On the spectral properties of shock-capturing schemes. *J. Comput. Phys.* **219** (2), 489–497.

POPE, S.B. 2000 *Turbulent Flows*. Cambridge University Press.

REESE, D.T., AMES, A.M., NOBLE, C.D., OAKLEY, J.G., ROTHAMER, D.A. & BONAZZA, R. 2018 Simultaneous direct measurements of concentration and velocity in the Richtmyer–Meshkov instability. *J. Fluid Mech.* **849**, 541–575.

RICHTMYER, R.D. 1960 Taylor instability in shock acceleration of compressible fluids. *Commun. Pure Appl. Maths* **13**, 297–319.

SHE, Z.-S. & LEVEQUE, E. 1994 Universal scaling laws in fully developed turbulence. *Phys. Rev. Lett.* **72**, 336–339.

SHE, Z.-S., REN, K., LEWIS, G.S. & SWINNEY, H.L. 2001 Scalings and structures in turbulent Couette–Taylor flow. *Phys. Rev.* E **64**, 016308.

SOULARD, O., GUILLOIS, F., GRIFFOND, J., SABELNIKOV, V. & SIMOËNS, S. 2018 Permanence of large eddies in Richtmyer–Meshkov turbulence with a small Atwood number. *Phys. Rev. Fluids* **3**, 104603.

SREENIVASAN, K.R. 2019 Turbulent mixing: a perspective. *Proc. Natl Acad. Sci. USA* **116** (37), 18175–18183.

SUN, Z.S., REN, Y.X., LARRICQ, C., ZHANG, S.Y. & YANG, Y.C. 2011 A class of finite difference schemes with low dispersion and controllable dissipation for DNS of compressible turbulence. *J. Comput. Phys.* **230** (12), 4616–4635.

TAM, C.K. & WEBB, J.C. 1993 Dispersion-relation-preserving finite difference schemes for computational acoustics. *J. Comput. Phys.* **107**, 262–281.

TAYLOR, G. 1950 The instability of liquid surfaces when accelerated in a direction perpendicular to their planes. I. *Proc. R. Soc. Lond.* A **201**, 192–196.

THORNBER, B., DRIKAKIS, D., YOUNGS, D.L. & WILLIAMS, R.J.R. 2010 The influence of initial condition on turbulent mixing due to Richtmyer–Meshkov instability. *J. Fluid Mech.* **654**, 99–139.

THORNBER, B., GRIFFOND, J., POUJADE, O., ATTAL, N., VARSHOCHI, H., BIGDELOU, P., RAMAPRABHU, P., OLSON, B., GREENOUGH, J., ZHOU, Y., *et al.* 2017 Late-time growth rate, mixing, and anisotropy in the multimode narrowband Richtmyer–Meshkov instability: the θ-group collaboration. *Phys. Fluids* **29** (10), 105107.

TOMKINS, C.D., BALAKUMAR, B.J., ORLICZ, G., PRESTRIDGE, K.P. & RISTORCELLI, J.R. 2013 Evolution of the density self-correlation in developing Richtmyer–Meshkov turbulence. *J. Fluid Mech.* **735**, 288–306.

TRITSCHLER, V.K., OLSON, B.J., LELE, S.K., HICKEL, S., HU, X.Y. & ADAMS, N.A. 2014*a* On the Richtmyer–Meshkov instability evolving from a deterministic multimode planar interface. *J. Fluid Mech.* **755**, 429–462.

TRITSCHLER, V.K, ZUBEL, M., HICKEL, S. & ADAMS, N.A. 2014*b* Evolution of length scales and statistics of Richtmyer–Meshkov instability from direct numerical simulations. *Phys. Rev.* E **90**, 063001.

VOROBIEFF, P., MOHAMED, N.-G., TOMKINS, C., GOODENOUGH, C., MARR-LYON, M. & BENJAMIN, R.F. 2003 Scaling evolution in shock-induced transition to turbulence. *Phys. Rev.* E **68**, 065301.

VOROBIEFF, P., RIGHTLEY, P.M. & BENJAMIN, R.F. 1998 Power-law spectra of incipient gas-curtain turbulence. *Phys. Rev. Lett.* **81**, 2240–2243.

WALCHLI, B. & THORNBER, B. 2017 Reynolds number effects on the single-mode Richtmyer–Meshkov instability. *Phys. Rev.* E **95**, 013104.

WATANABE, T. & GOTOH, T. 2004 Statistics of a passive scalar in homogeneous turbulence. *New J. Phys.* **6** (1), 40.

WEBER, C., HAEHN, N., OAKLEY, J., ROTHAMER, D. & BONAZZA, R. 2012 Turbulent mixing measurements in the Richtmyer–Meshkov instability. *Phys. Fluids* **24**, 074105.

WONG, M.L., BALTZER, J.R., LIVESCU, D. & LELE, S.K. 2022 Analysis of second moments and their budgets for Richtmyer–Meshkov instability and variable-density turbulence induced by reshock. *Phys. Rev. Fluids* **7**, 044602.

WONG, M.L. & LELE, S.K. 2017 High-order localized dissipation weighted compact nonlinear scheme for shock-and interface-capturing in compressible flows. *J. Comput. Phys.* **339**, 179–209.

WONG, M.L., LIVESCU, D. & LELE, S.K. 2019 High-resolution Navier–Stokes simulations of Richtmyer–Meshkov instability with reshock. *Phys. Rev. Fluids* **4**, 104609.

YAN, Z., FU, Y., WANG, L., YU, C. & LI, X. 2022 Effect of chemical reaction on mixing transition and turbulent statistics of cylindrical Richtmyer–Meshkov instability. *J. Fluid Mech.* **941**, A55.

YEUNG, P.K. & POPE, S.B. 1989 Lagrangian statistics from direct numerical simulations of isotropic turbulence. *J. Fluid Mech.* **207**, 531–586.

YOUNGS, D.L. 2004 Effect of initial conditions on self-similar turbulent mixing. In *Proceedings of the International Workshop on the Physics of Compressible Turbulent Mixing* (ed. S.B. Dalziel), vol. 9, 122.

ZHAO, Z., LIU, N.-S. & LU, X.-Y. 2020 Kinetic energy and enstrophy transfer in compressible Rayleigh–Taylor turbulence. *J. Fluid Mech.* **904**, A37.

ZHOU, Y. 2001 A scaling analysis of turbulent flows driven by Rayleigh–Taylor and Richtmyer–Meshkov instabilities. *Phys. Fluids* **13** (2), 538–543.

ZHOU, Y. 2017 Rayleigh–Taylor and Richtmyer–Meshkov instability induced flow, turbulence, and mixing. II. *Phys. Rep.* **723–725**, 1–160.

ZHOU, Y., WILLIAMS, R.J.R., RAMAPRABHU, P., GROOM, M., THORNBER, B., HILLIER, A., MOSTERT, W., ROLLIN, B., BALACHANDAR, S., POWELL, P.D., *et al.* 2021 Rayleigh–Taylor and Richtmyer–Meshkov instabilities: a journey through scales. *Physica* D **423**, 132838.

ZHOU, Z., DING, J., HUANG, S. & LUO, X. 2023 A new type of weighted compact nonlinear scheme with minimum dispersion and adaptive dissipation for compressible flows. *Comput. Fluids* **262**, 105934.